



Homogenized transition conditions for plasmonic metasurfaces

Nicolas Lebbe, Agnes Maurel, Kim Pham

► To cite this version:

Nicolas Lebbe, Agnes Maurel, Kim Pham. Homogenized transition conditions for plasmonic metasurfaces. Physical Review B, 2023, 107 (8), pp.085124. 10.1103/PhysRevB.107.085124 . hal-03989215

HAL Id: hal-03989215

<https://hal.science/hal-03989215>

Submitted on 14 Feb 2023

HAL is a multi-disciplinary open access archive for the deposit and dissemination of scientific research documents, whether they are published or not. The documents may come from teaching and research institutions in France or abroad, or from public or private research centers.

L'archive ouverte pluridisciplinaire **HAL**, est destinée au dépôt et à la diffusion de documents scientifiques de niveau recherche, publiés ou non, émanant des établissements d'enseignement et de recherche français ou étrangers, des laboratoires publics ou privés.

Homogenized transition conditions for plasmonic metasurfacesNicolas Lebbe^{1,*} and Agnès Maurel*Institut Langevin, ESPCI Paris, Université PSL, Sorbonne Université, Université de Paris, CNRS, 75005 Paris, France*

Kim Pham

IMSIA, CNRS, EDF, CEA, ENSTA Paris, Institut Polytechnique de Paris, 828 Boulevard des Maréchaux, 91732 Palaiseau, France

(Received 16 August 2022; revised 31 January 2023; accepted 2 February 2023; published 14 February 2023)

The present study aims to model the optical response of plasmonic metasurfaces made of a periodic arrangement of metallic particles with arbitrary shape and subwavelength dimensions. By combining homogenization with quasistatic plasmonic eigenmode expansion, the metasurface is replaced by a zero-thickness interface associated with frequency-dependent effective susceptibilities. The resulting discontinuities of the fields are responsible for strong interaction with the incoming light at the resonances when the complex permittivity of the metal passes close to the real permittivity of an eigenmode. Our modeling provides a physical picture of resonances in plasmonic metasurfaces, and it allows for a huge decrease in the numerical cost of their computations. In addition, comparisons with direct numerics in two dimensions evidence its predictive force at any incidence, particle shape, and arrangement.

DOI: [10.1103/PhysRevB.107.085124](https://doi.org/10.1103/PhysRevB.107.085124)**I. INTRODUCTION**

Localized surface plasmon resonances (LSPRs) in subwavelength metallic particles are associated with static eigenmodes characterized by high confinement of the fields at the particle boundary and large evanescence when moving away from it [1]. In practice, resonances of a single particle are significantly affected by Ohmic losses due to Drude-type dispersion in metals resulting in weak interaction with the incoming light. This drawback has been overcome using plasmonic metasurfaces for which the couplings between particles modify the characteristics of the resonances [2,3]. For a period on the wavelength scale or greater, diffractively coupled LSPRs give rise to plasmonic surface lattice resonances. For a subwavelength period, enhanced resonances are produced by the near-field couplings between neighboring particles. In general, they result in large Q factors [4–6], which have been exploited for several applications, including thin efficient absorbers [7,8], plasmonic sensors [9], reconfigurable flat metalenses [10], and phase graded metasurface holograms in the visible range [11,12].

From a theoretical perspective, pioneering works starting in the 1960s proposed electric dipole models that exhibit effective susceptibilities arising from the localized plasmonic modes; see the review in [3]. The coupled-dipole or discrete-dipole approximation aims to model a metasurface as a collection of independent scattering particles characterized by their static polarizability, an approximation which is well adapted for small particles and large array periods [13,14]. Among the exact numerical methods, those based on modal expansions for the rigorous coupled-wave analysis rely on

Fourier expansions of the fields. Having in mind the idea that the optical response of resonant metasurfaces results from the excitation of just a few modes, Lalanne and coworkers proposed to use expansions of the fields in terms of quasinormal modes, which uses the leaky eigenmodes of Maxwell's equations [15,16]; see the review in [17]. For metasurfaces with subwavelength period and thickness and having some underlying homogenization process in mind, several authors considered using a metasurface with effective transition conditions involving surface impedances or surface susceptibilities. Starting with the pioneering work of Idemen [18], these generalized sheet transition conditions (GSTCs) have been popularized in their most general form. We mention the few works in which the homogenization process leading to GSTCs is explicit [19–24].

Our work starts with the observation that LSPRs, in contrast to most resonances, e.g., Mie resonances, do not rely on a dynamic mechanism. They are found as static solutions of source-free electrostatic equations for given real, negative permittivity values [1]. From a homogenization perspective, this means that they will be captured within the framework used for nonresonant particles, as recently proposed for the full Maxwell's equations [24]. This could be sufficient; however, an annoying drawback of the resulting formulation is that the effective susceptibilities depend on the permittivity of the metal. Hence, when Drude's law is accounted for, they depend *a posteriori* on the frequency, which requires the associated static elementary problems to be solved at each permittivity in the considered frequency range. This is overcome using a modal decomposition based on the eigenmodes of a periodic plasmonic eigenvalue problem (PEP) in the quasistatic limit [23,25]. The procedure is presented in Sec. II for two-dimensional settings, and the predictive force of the resulting model is exemplified in Sec. III.

*lebbe.nicolas@gmail.com

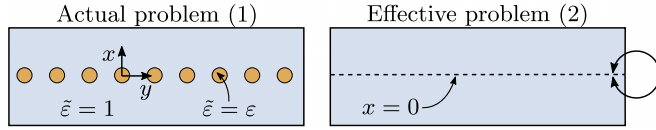


FIG. 1. The actual problem ruled by (1) (left) and the effective problem (right) ruled by transition conditions (2).

II. THE EFFECTIVE MODEL

A. Summary: The actual problem and the effective problem

We consider a metasurface made of metallic particles invariant along z (Fig. 1, left panel) and polarized waves with magnetic field $\mathbf{H} = H(\mathbf{x})\mathbf{e}_z$, $\mathbf{x} = (x, y)$, governed by

$$\text{Actual problem: } \begin{cases} \nabla \cdot \left(\frac{1}{\tilde{\epsilon}(\mathbf{x})} \nabla H \right) + k^2 H = 0, \\ H \text{ and } \frac{1}{\tilde{\epsilon}} \nabla H \cdot \mathbf{n} \text{ continuous,} \end{cases} \quad (1)$$

where $\tilde{\epsilon}(\mathbf{x})$ is the relative permittivity which depends on space ($\tilde{\epsilon} = 1$ in the air and $\tilde{\epsilon} = \epsilon$ in the metal) and $k = \sqrt{\epsilon_0 \mu_0} \omega$ is the wave number in the air (ω is the angular frequency). We restrict our study to particle shapes symmetric with respect to $y = 0$ in the unit cell, which slightly simplifies the problem without missing the physical mechanisms. Below, we show that the array can be replaced by an equivalent interface ruled by effective transition conditions (GSTCs) of the form (Fig. 1, right panel)

$$\text{Effective problem: } \begin{cases} \Delta H + k^2 H = 0, \\ \llbracket H \rrbracket = \chi^y \partial_x \bar{H}, \\ \llbracket \partial_x H \rrbracket = \chi^x \partial_{yy} \bar{H}, \end{cases} \quad (2)$$

where, with $H^\pm = H(0^\pm, y)$, $\llbracket H \rrbracket = H^+ - H^-$ and $\bar{H} = \frac{1}{2}(H^+ + H^-)$ are the jump and the mean value of H across the equivalent interface at $x = 0$. The effective susceptibilities entering (2) read

$$\chi^x = d \sum_n \frac{(\chi_n^x)^2}{1 - \frac{\epsilon_n}{\epsilon}} + d\varphi \left(1 - \frac{1}{\epsilon} \right), \quad \chi^y = d \sum_n \frac{(\chi_n^y)^2}{1 - \frac{\epsilon_n}{\epsilon}}, \quad (3)$$

where d is the array spacing and $\varphi = S/d^2$ is the particle cross section S normalized with d^2 (for several particles in the unit cell, S is the sum of their sections). The effective surface susceptibilities (χ^x, χ^y) are the diagonal terms of the electric susceptibility tensor entering the GSTCs recently derived for Maxwell's equations [24]. In (3), the susceptibilities are defined by introducing a discrete set of real, negative eigenvalues ϵ_n of the periodic PEP and the weights (χ_n^x, χ_n^y) that are specified in Sec. II C [see (17) and (19)].

B. Homogenization

Following [21,26], (1) is rewritten in the form

$$\nabla \cdot \mathbf{C} + k^2 H = 0, \quad \mathbf{C} = \frac{1}{\tilde{\epsilon}} \nabla H, \quad (4)$$

with the boundary conditions being now the continuities of H and of $\mathbf{C} \cdot \mathbf{n}$ at the metal-air interfaces. We notice that the electric field $\mathbf{E} = (E_x, E_y, 0)$ is linked to \mathbf{C} , as we have

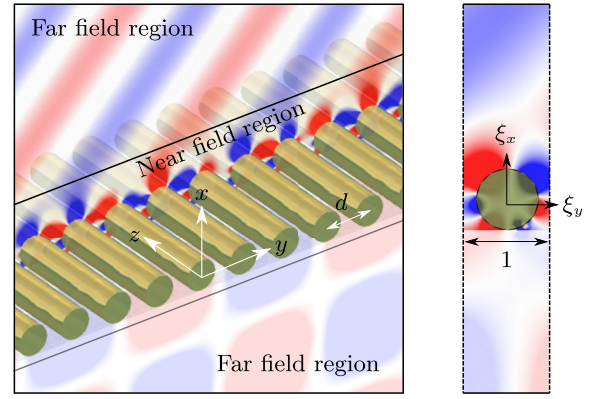


FIG. 2. Near- and far-field regions used in the asymptotic analysis (left) and the elementary cell in rescaled coordinates (right).

$C_x = i\omega E_y$ and $C_y = -i\omega E_x$ (the normal component of \mathbf{C} corresponds to the tangential component of \mathbf{E}). The effective model is derived owing to matched asymptotic techniques combined with two-scale homogenization owing to the small parameter $\delta = kd \ll 1$, with d being the array period, in the low-frequency regime (in the following, without loss of generality, we set $k = 1$, and hence, $\delta = d$). In addition to the macroscopic coordinate \mathbf{x} which measures variations of the fields on the wavelength scale, we define the microscopic coordinate $\boldsymbol{\xi} = \frac{\mathbf{x}}{d}$, $\boldsymbol{\xi} = (\xi_x, \xi_y)$, which measures variations of the fields on the (small) scale d , typically those of the evanescent field (see Fig. 2).

1. Analysis of the far field

In the air far from the array, the fields have slow variations, at the wavelength scale; hence, they depend on only \mathbf{x} . We require the solution to be approximated by

$$H(\mathbf{x}, y) \underset{x \rightarrow 0^\pm}{\sim} H(0^\pm, y) + x \partial_x H(0^\pm, y). \quad (5)$$

With $x = d\xi_x$ and introducing the jump $\llbracket H \rrbracket = d[H]$ and the mean value of H as in (2), we have

$$H(\mathbf{x}, y) \underset{x \rightarrow 0^\pm}{\sim} \bar{H}(y) + d(\xi_x \partial_x \bar{H}(y) \pm \frac{1}{2} [H](y)), \quad (6)$$

the same as for \mathbf{C} . Eventually, we notice that, in the air, $\mathbf{C} = \nabla H$.

2. Analysis of the near field

The near-field region is the region of the array including the evanescent fields, and it is the most challenging part of the analysis. There, the fields have rapid variations which are accounted for by $\boldsymbol{\xi}$ and slow variations when moving along the array in the y direction. Accordingly, we use the expansions

$$\begin{aligned} H &= h^{(0)}(\boldsymbol{\xi}, y) + dh^{(1)}(\boldsymbol{\xi}, y) + \dots, \\ \mathbf{C} &= \mathbf{c}^{(0)}(\boldsymbol{\xi}, y) + d\mathbf{c}^{(1)}(\boldsymbol{\xi}, y) + \dots, \end{aligned} \quad (7)$$

and we need only the first two orders in the expansions. The terms in the expansions are assumed to be periodic with respect to $\xi_y \in (-\frac{1}{2}, \frac{1}{2})$. Note that the elementary cell is unbounded along ξ_x , but the fields in (6) and in (7) have to match in an intermediate region where $\xi_x \rightarrow \pm\infty$ while

$x \rightarrow 0^\pm$, namely, when $d \ll |x| \ll 1$ (with $k = 1$ still). Eventually, in the near-field region, the differential operator reads $\nabla \rightarrow \frac{1}{d}\nabla_\xi + \mathbf{e}_y\partial_y$, which is used in (4) to get

$$\frac{1}{d}\nabla_\xi \cdot \mathbf{C} + \partial_y C_y + H = 0, \quad \mathbf{C} = \frac{1}{\tilde{\varepsilon}} \left(\frac{1}{d}\nabla_\xi H + \partial_y H \mathbf{e}_y \right), \quad (8)$$

with $\tilde{\varepsilon} = \tilde{\varepsilon}(\xi)$. Inserting the expansions in (7) in (8) and identifying the terms with the same power in d , we find at the dominant order in $\frac{1}{d}$ that $\nabla_\xi h^{(0)} = \mathbf{0}$; hence, $h^{(0)}$ does not depend on ξ . Identifying the dominant term of H in (6) and (7), we deduce that

$$h^{(0)}(y) = \overline{H}(y). \quad (9)$$

We now move to the problem satisfied by $(\mathbf{c}^{(0)}, h^{(1)})$. We use (8) along with (9), and we identify $\mathbf{c}^{(0)}$ in (7) when $\xi_x \rightarrow \pm\infty$ with $\overline{\mathbf{C}}$ in (6). Using $\overline{C}_y = \partial_y \overline{H}$, we obtain

$$\begin{aligned} \nabla_\xi \cdot \mathbf{c}^{(0)} &= 0, \quad \mathbf{c}^{(0)} = \frac{1}{\tilde{\varepsilon}} (\nabla_\xi h^{(1)} + \partial_y \overline{H}(y) \mathbf{e}_y), \\ \lim_{\xi_x \rightarrow \pm\infty} \mathbf{c}^{(0)} &= \overline{C}_x(y) \mathbf{e}_x + \partial_y \overline{H}(y) \mathbf{e}_y, \end{aligned} \quad (10)$$

with $h^{(1)}$ being continuous and ξ_y -periodic, and $\mathbf{c}^{(0)} \cdot \mathbf{n}$ being continuous and ξ_y -antiperiodic. We shall now use the fact that the above problem, set in $\Omega = \{\xi_x \in (-\infty, \infty), \xi_y \in (-\frac{1}{2}, \frac{1}{2})\}$, is linear with respect to \overline{C}_x and $\partial_y \overline{H}$. Hence, we can set

$$h^{(1)}(\xi, y) = \overline{C}_x(y)(Q_y(\xi) + \xi_x) + \partial_y \overline{H}(y)Q_x(\xi), \quad (11)$$

with Q_x and Q_y being the solutions to the elementary problems

$$\begin{aligned} \nabla_\xi \cdot \left(\frac{1}{\tilde{\varepsilon}} (\nabla_\xi Q_x + \mathbf{e}_y) \right) &= 0, \quad \lim_{\xi_x \rightarrow \pm\infty} \nabla_\xi Q_x = \mathbf{0}, \quad \text{in } \Omega, \\ \nabla_\xi \cdot \left(\frac{1}{\tilde{\varepsilon}} (\nabla_\xi Q_y + \mathbf{e}_x) \right) &= 0, \quad \lim_{\xi_x \rightarrow \pm\infty} \nabla_\xi Q_y = \mathbf{0}, \quad \text{in } \Omega, \end{aligned} \quad (12)$$

for $t = x, y$, Q_t being ξ_y -periodic and continuous and $\frac{1}{\tilde{\varepsilon}}(\nabla_\xi Q_t + \mathbf{e}_t) \cdot \mathbf{n}$ being ξ_y -antiperiodic and continuous. In particular, we have

$$Q_x \underset{\xi_x \rightarrow \pm\infty}{\sim} 0, \quad Q_y \underset{\xi_x \rightarrow \pm\infty}{\sim} \pm \frac{\chi^y}{2d} \quad (13)$$

(we used the fact that, when symmetric shapes are considered, Q_x is antisymmetric under the transformation $\xi_y \rightarrow -\xi_y$, which means that the constants at infinity are zero). The limits in (13) can be used in (11) to find $h^{(1)}$ when $\xi_x \rightarrow \pm\infty$, namely, $h^{(1)} \sim \overline{C}_x(y)(\xi_x \pm \frac{\chi^y}{2d})$. Identifying now the terms in d in (6) and (7) provides $\llbracket H \rrbracket = d[H]$ of the form

$$\llbracket H \rrbracket(y) = \chi^y \overline{C}_x(y), \quad (14)$$

which corresponds to the first jump announced in (2). We now look for the jump of C_x which is provided by the first relation in (8) at the order d^0 : $(\nabla_\xi \cdot \mathbf{c}^{(1)} + \partial_y c_y^{(0)} + \overline{H}) = 0$, which we integrate over Ω . Making use of the divergence theorem makes $\llbracket C_x \rrbracket$ appear, and using the form of $c_y^{(0)}$ in (10), along with (11), in the second integral provides the jump of C_x of the form indicated in (2),

$$\llbracket C_x \rrbracket(y) = \chi^x \partial_{yy} \overline{H}(y), \quad (15)$$

where

$$\chi^x = -d \int_\Omega \frac{\partial_{\xi_y} Q_x}{\tilde{\varepsilon}} d\xi + d\varphi \left(1 - \frac{1}{\varepsilon} \right) \quad (16)$$

(we have used the fact that Q_y is symmetric under $\xi_y \rightarrow -\xi_y$, resulting in $\int_\Omega (\partial_{\xi_y} Q_y / \tilde{\varepsilon}) d\xi = 0$).

C. Periodic plasmonic eigenmode decomposition

From the preceding section, the effective susceptibilities entering (2) are obtained by solving elementary problems (12) depending on ε (among other things such as the particle shape). In practice, ε varies with the frequency, which would require the susceptibilities to be calculated in the whole range of working frequencies and hence would make the effective model less attractive. To avoid this drawback, we use a decomposition of the elementary problems by exploiting the plasmonic eigenmodes $q_n(\xi)$ and the associated eigenvalues ε_n , the solutions to the periodic PEP,

$$\nabla_\xi \cdot \left(\frac{1}{\tilde{\varepsilon}} \nabla_\xi q_n \right) = 0, \quad \lim_{\xi_x \rightarrow \pm\infty} \nabla_\xi q_n = \mathbf{0}, \quad \text{in } \Omega, \quad (17)$$

with q_n being continuous and ξ_y -periodic, and $\frac{1}{\tilde{\varepsilon}} \nabla_\xi q_n \cdot \mathbf{n}$ being continuous and ξ_y -antiperiodic [23,25]; in addition, $\tilde{\varepsilon} = 1$ in the air, and $\tilde{\varepsilon} = \varepsilon_n$ in the metal. It should be noted that this type of decomposition of the permittivity has already been studied many times in the literature [27–29], notably with an extension to the dynamic case in, for instance, Refs. [30,31], in which complex eigenvalues are obtained. We notice that this eigenvalue problem is the sourceless version of the elementary problems (12) (hence, q_n can be symmetric or antisymmetric). Multiplying (17) by q_m and integrating by parts, we obtain the orthogonality relation of the normalized eigenmodes $\int_{\Omega_a} \nabla_\xi q_n \cdot \nabla_\xi q_m d\xi = \delta_{mn}$ and the associated eigenvalues

$$\varepsilon_n = - \int_{\Omega_m} |\nabla_\xi q_n|^2 d\xi, \quad (18)$$

where $\Omega_{a,m}$ are the regions of air and of metal ($\Omega = \Omega_m \cup \Omega_a$). Next, from (17), along with (13) and (16), we define

$$q_n(\xi) \underset{\xi_x \rightarrow \pm\infty}{\sim} \pm \frac{1}{2} \chi_n^y, \quad \chi_n^x = - \int_\Omega \frac{\partial_{\xi_y} q_n}{\tilde{\varepsilon}} d\xi, \quad (19)$$

with $\chi_n^y = 0$ for symmetric modes and $\chi_n^x = 0$ for antisymmetric modes. The modal decomposition of Q_y and Q_x , owing to (12), provides for $t = x, y$,

$$Q_t(\xi) = \sum_n \alpha_n^t q_n(\xi), \quad \alpha_n^t = \frac{\chi_n^t}{1 - \varepsilon_n / \varepsilon}. \quad (20)$$

By linearity, we also have $\chi^x/d = \sum \alpha_n^x \chi_n^x + \varphi(1 - 1/\varepsilon)$ and $\chi^y/d = \sum \alpha_n^y \chi_n^y$, from which we deduce the forms announced in (3). The validation of the PEP is reported in Fig. 3. We computed (χ^x, χ^y) (a) directly from (13) and (16), which requires the resolution of the elementary problems (12) for each value of ε within a given range, and (b) by solving, once and for all, the plasmonic eigenvalue problem (17) and selecting values falling within the same range of ε . This single calculation provides ε_n and (χ_n^x, χ_n^y) in (19) that are used in (3). We notice the accumulation of eigenmodes near $\varepsilon = -1$,

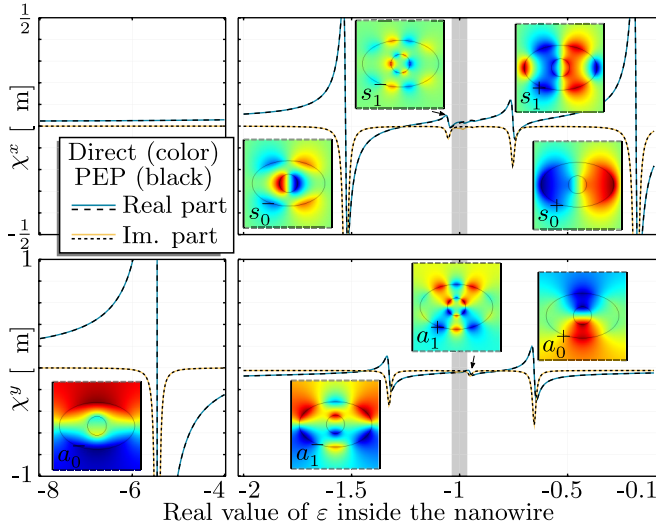


FIG. 3. Efficiency of the modal expansion using the plasmonic eigenvalue problem (PEP), with a direct calculation from the resolution of (13) and (16).

corresponding to the eigenvalue of a circular cylinder in free space [32]; additional information is given in the Appendix. These sharp resonances are smoothed when adding a small imaginary part to ε (for readability we used $\text{Im } \varepsilon = 10^{-2}$).

III. VALIDATION OF THE EFFECTIVE MODEL

A. Scattering of an incident plane wave

To validate our effective model, we consider the scattering of an incident plane wave at oblique incidence θ on the array, for which the solution to the effective problem (2) reads

$$\begin{aligned} H(x < 0, y) &= H_0(e^{ik \cos \theta x} + r e^{-ik \cos \theta x})e^{ik \sin \theta y}, \\ H(x > 0, y) &= H_0 t e^{ik \cos \theta x} e^{ik \sin \theta y}, \end{aligned} \quad (21)$$

and using the transition conditions in (2), (r, t) is given by

$$r = \frac{1}{2} \left(\frac{z_1}{z_1^*} - \frac{z_2}{z_2^*} \right), \quad t = \frac{1}{2} \left(\frac{z_1}{z_1^*} + \frac{z_2}{z_2^*} \right), \quad (22)$$

with $z_1 = \cos \theta + i \frac{k}{2} \chi^x \sin^2 \theta$ and $z_2 = 1 + i \frac{k}{2} \chi^y \cos \theta$. In the absence of losses, χ^x and χ^y are real, and z_n^* denotes the complex conjugate of z_n , $n = 0, 1$, and $|r|^2 + |t|^2 = 1$, as expected. In contrast, when losses are accounted for, χ^x and χ^y are complex, and $z_1^* = \cos \theta - i \frac{k}{2} \chi^x \sin^2 \theta$, and $z_2^* = 1 - i \frac{k}{2} \chi^y \cos \theta$.

To illustrate the role of the plasmonic eigenmodes, we fix the wavelength to an arbitrary constant value ($\lambda = 1 \mu\text{m}$), and we inspect the variations of the transmission $|t|^2$ against the real part of ε . The result, reported in Fig. 4, shows excellent agreement between the Finite Element Method (FEM) calculation and the transmission predicted by (22). In particular, antisymmetric resonances are excited only at oblique incidence, being prevented by symmetry at normal incidence. Indeed, symmetric resonances, with large χ^y , produce $z_1/z_1^* \sim 1$ and $z_2/z_2^* \sim -1$; similarly, antisymmetric resonances, with large χ^x , produce $z_1/z_1^* \sim -1$ and $z_2/z_2^* \sim 1$ if $\theta \neq 0$. It results in transmission dips at the four symmetric resonances

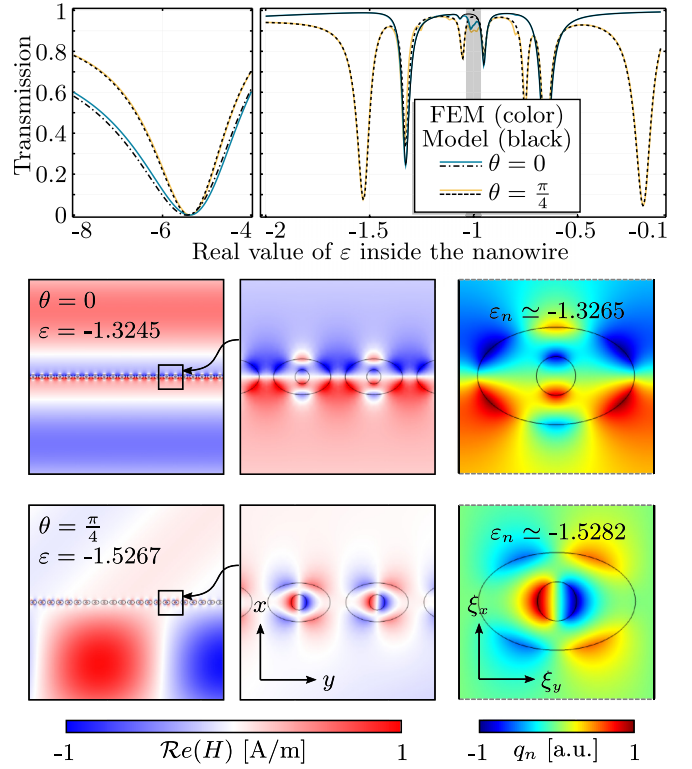


FIG. 4. Top panels: Transmission against the real value of ε . Bottom panels: Fields H near two resonances; the right panels show the closest plasmonic eigenmodes a_1^- and s_0^- (see Fig. 3).

for $\theta = 0$ and four additional dips at the four antisymmetric resonances for $\theta = \pi/4$ (the shapes of the corresponding eigenmodes are shown Fig. 3). We also report the scattering patterns of the magnetic field in the vicinity of resonances a_1^- and s_0^- (Fig. 4, bottom, left and middle panels). Unsurprisingly, the wave fields within the metasurface resemble (up to a phase term) that of the closest eigenmode (Fig. 4, bottom, right panels).

B. Dispersion and losses

From now on, we account for the Lorentz-Drude law which renders the resonances frequency (or wavelength) dependent through $\varepsilon(\omega)$,

$$\varepsilon(\omega) = 1 - \sum_{j=0}^5 \frac{f_j \omega_p^2}{(\omega^2 - \omega_j^2) - i \omega \Gamma_j}, \quad (23)$$

with the plasmon frequency $\omega_p = 9.03 \text{ eV}$ and with the values of $(f_j, \omega_j, \Gamma_j)$, $j = 0, \dots, 5$ in Table I.

However, in order to clearly illustrate the predictive force of our model, we take the liberty to decrease the losses artificially by a factor of 100 in the next section.

1. Example with artificially low losses

To begin with, we report in Fig. 5 the patterns of the magnetic field for $\lambda = 551 \text{ nm}$ and $\lambda = 454 \text{ nm}$ in the vicinity of the resonances attributable to a_1^- and s_1^- . The solution to the actual problem is shown for $y < 0$, and the solution to the effective problem is shown for $y > 0$ for the same

TABLE I. Parameters of the Lorentz-Drude model for gold and silver in the visible spectrum from [33]. The values are multiplied by $1 \text{ eV}/\hbar \sim 1.519 \cdot 10^{15}$ when used in (23).

	n					
	0	1	2	3	4	5
Gold						
f_n	0.760	0.024	0.010	0.071	0.601	4.384
Γ_n	0.053	0.241	0.345	0.870	2.494	2.214
ω_n	0	0.415	0.830	2.969	4.304	13.32
Silver						
f_n	0.845	0.065	0.124	0.011	0.840	5.646
Γ_n	0.048	3.886	0.452	0.065	0.916	2.419
ω_n	0	0.816	4.481	8.185	9.083	20.29

incident wave. In the numerics the apparent discontinuity of the field across the array of particles results from progressive variations, over short distances, due to the evanescent field triggered by the particles (this is particularly visible in the top panel of Fig. 5 with a phase jump of about $\pi/2$). In the model, the discontinuity is sudden (at $x = 0$), and it results from the transition conditions (2). A salient consequence, illustrated by the magnifications near the metasurface, is that the variations of the magnetic field near the particles are not reproduced in the effective problem, and this is expected. Indeed, this “near-field” region sketched in Fig. 2 has disappeared in the asymptotic analysis. However, as expected, the resulting sudden discontinuities of the fields (rather than progressive, through the evanescent field) allow the far fields to be faithfully reproduced.

More quantitatively, we have numerically computed the transmission coefficient t while varying both the incidence angle θ and the wavelength. A comparison of the amplitude and

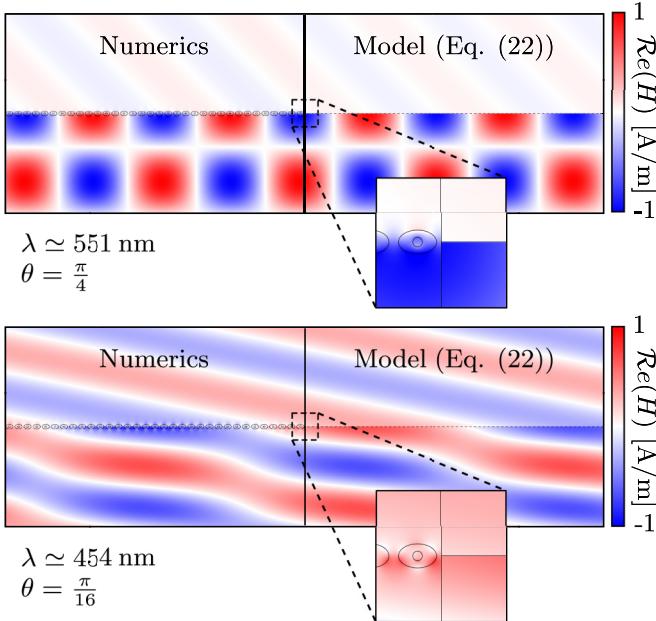


FIG. 5. Field H solution to the actual and effective problems; the insets highlight the role of the transition conditions (2) responsible for the field discontinuities.

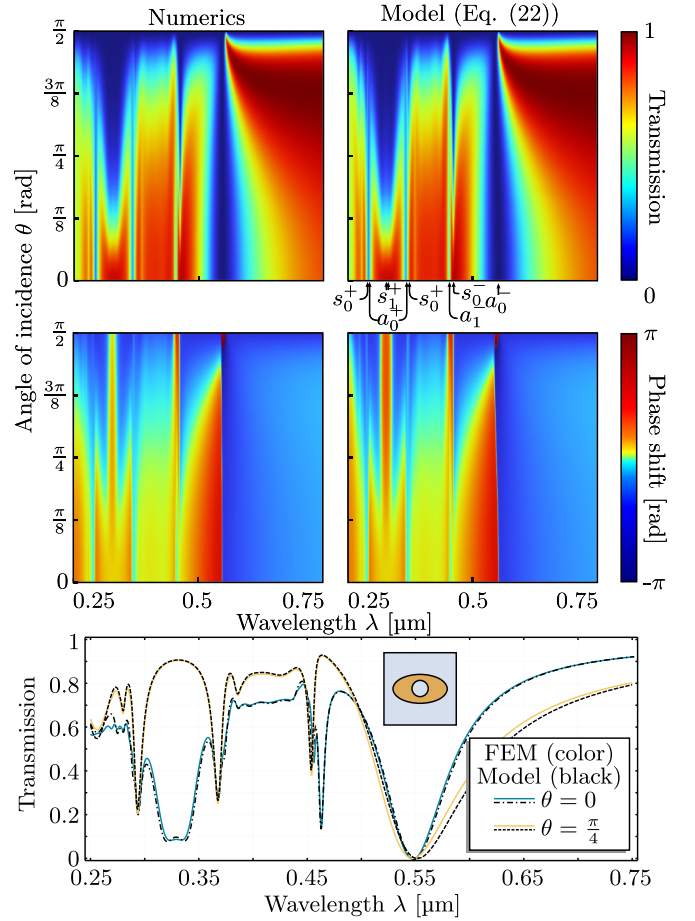


FIG. 6. Transmission $|t|^2$ and phase of t against θ and λ (top and middle panels) and profiles of $|t|^2$ for $\theta = 0, \pi/4$ (bottom panels). Artificial low losses are considered (see text).

phase of t with our prediction (22) is reported in Fig. 6 (top and middle panels); the agreement is further quantified in the profiles at $\theta = 0$ and $\pi/4$ (bottom panel). The spectrum exhibits transmission dips within small frequency ranges with a weak, although visible, dependence on the incident angle. As previously noted, these dips are dictated by the symmetric and antisymmetric resonances at a specific frequency. We notice in addition an almost perfect transmission for $\lambda > 0.55 \mu\text{m}$ with weak dependence on $\theta \in (0.37\pi, 0.5\pi)$, corresponding to the impedance matching condition at the Brewster angle given by

$$\tan^2 \theta = \chi^y / \chi^x, \quad (24)$$

as already observed in the context of metamaterials [34].

The numerical and theoretical spectra are represented using the same resolution in λ (1 nm) and θ ($\pi/1000$) needed to find the strongest resonances and in the numerics; in addition, a high-quality mesh is necessary to resolve the variations of the evanescent field triggered in the vicinity of the particles. The result is that the increase in the computation cost is huge. For the 500^2 direct FEM simulations, the computation time is about 18 h (~ 0.23 s per simulation). In contrast, the model provides the analytical form of t in (22); hence, the computational cost is reduced to the resolution of the PEP, which in the reported case is about 10 s. We notice that the computation

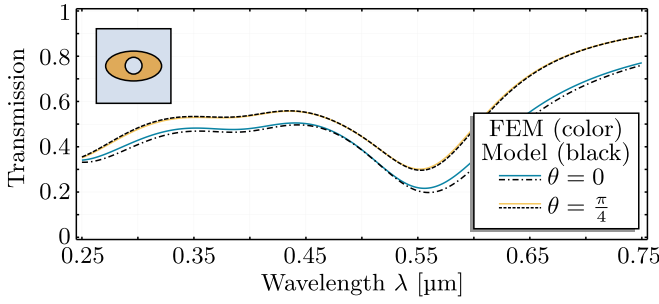


FIG. 7. Transmission profiles accounting for the actual losses from Table I; the representation is the same as in Fig. 6, bottom panel.

increase will be even more significant in three dimensions as t will still be explicit in the model.

2. From artificially low to actual losses in metals

We now move to the actual losses from Table I resulting in the transmission profiles reported in Fig. 7. As expected, the resonances with high quality factors for $0.25 < \lambda < 0.5 \mu\text{m}$ are more affected by the losses. As a result, the strong variations in the transmission observed in Fig. 6 are considerably weakened, and a single flat-banded one remains noticeable near $\lambda = 0.55 \mu\text{m}$, associated with the eigenmode a_0^- (with $\text{Re}(\epsilon) \sim -5.5$). In contrast, the transmission is now almost constant for wavelengths shorter than $0.5 \mu\text{m}$; however, omitting the presence of the resonant eigenmodes in this frequency range cause the observed, relatively low transmission to be overlooked.

In practice, plasmonic resonances are sensitive to any change in the geometry, in particular to the array spacing, as characterized experimentally in [35]. Following this reference, we considered circular gold particles with a radius of 10 nm with spacing d between 21 nm (1 nm between two particles) and 45 nm (25 nm between two particles). The transmissions through such arrays are reported in Fig. 8. The overall variations are similar to those of eye-shaped particles, but expectedly, we notice that the main dip in transmission

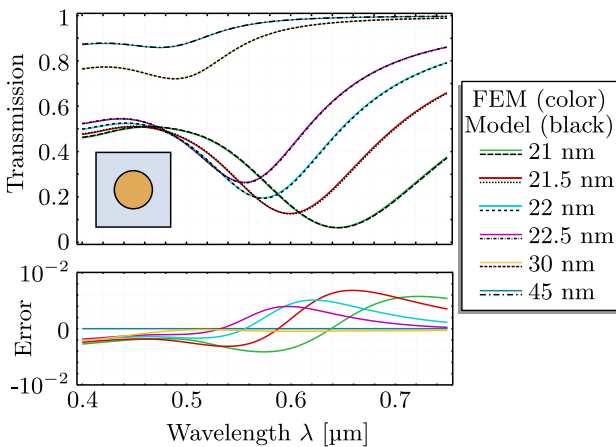


FIG. 8. Influence of the array spacing $d \in (21, 45)$ nm for a circular gold particle with a radius of 10 nm. Transmission profiles $|r|^2$ at $\theta = \pi/4$ for different spacings (top panel) and absolute errors between $|r|^2$ in the model and in the FEM numerics (bottom panel).

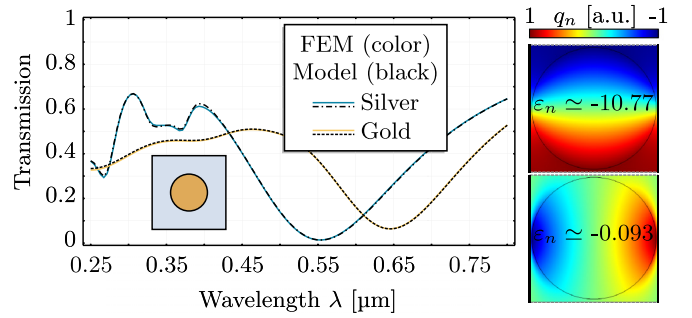


FIG. 9. Left: Transmission at $\theta = \pi/4$ for circular particles with a radius of 10 nm with array spacing $d = 21$ nm with two different materials. Right: Highest and lowest modes associated with the circular particle.

is sensitive to the particle shape, moving from $\lambda = 0.55 \mu\text{m}$ to $\lambda = 0.48 \mu\text{m}$ for the same periodicity $d = 50$ nm. Next, the high precision of the model provides faithful predictions of the transmission curves, with an increasing impact of the metasurface due to increasing near-field effects accompanied by redshifts of the resonance frequency (the absolute error is less than 10^{-2} in the reported cases).

Finally, we emphasize the fact that the plasmonic eigenmodes do not depend on the dispersion relation of ϵ by showing in Fig. 9 that the same modes can be used to compute the effective model associated with particles having the same geometry but different materials. It should also be noted that for periodic particles made of multiple constituents, it is necessary to modify the PEP and the modal expansion as proposed in [36]. Similarly, adaptations can be made in order to deal with a spatially varying permittivity profile inside the meta-atom [37].

C. Accuracy and limitations of the homogenized model

In this section, we provide a more in-depth analysis of the accuracy and limitations of our model. As explained earlier, the effective transition condition should work as soon as the fields near the meta-atoms can be described by their quasistatic response, i.e., in the subwavelength regime. We have numerically analyzed the accuracy of our model as a function of λ/d (d is the period of the metasurface, and its thickness is assumed to be of the same order of magnitude). To do this, we numerically calculated the scattering coefficients (r^{num} , t^{num}) of a metasurface as a function of λ/d ; we considered two shapes of gold or silver meta-atoms and two angles of incidence, $\theta = 0$ and $\theta = \pi/4$. The results are shown in Fig. 10. The reported errors correspond to $|r - r^{\text{num}}|$ and $|t - t^{\text{num}}|$, with (r, t) given by (22). In all cases, the error decreases in $(\lambda/d)^{-2}$, which is expected since the asymptotic analysis was conducted up to order 1. These results tell us, moreover, that surface homogenization of plasmonic metasurfaces gives good results (with an error below a few percent) for any angle of incidence if d does not exceed $\sim \lambda/10$. In the specific case of optics, this means that one can expect an accurate response in the visible spectrum at any angle of incidence for periodicity patterns of the order of (or smaller than) 50 nm.

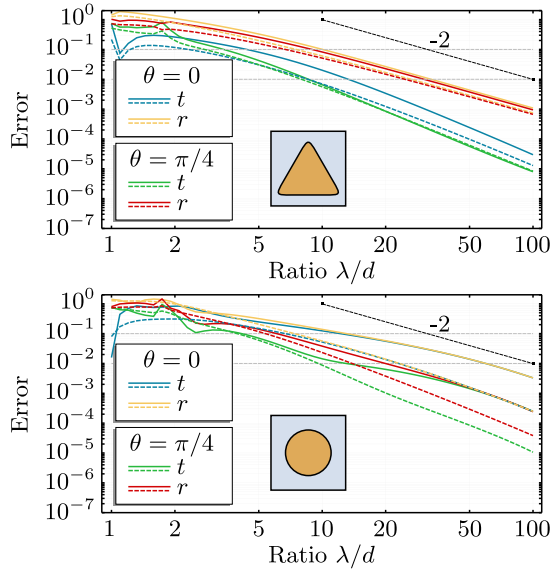


FIG. 10. Error $|r - r^{\text{num}}|$ and $|t - t^{\text{num}}|$ as a function of λ/d for $\theta = 0$ (blue and yellow curves) and $\theta = \pi/4$ (green and red curves). The solid (dashed) lines correspond to the meta-atom consisting of silver (gold) at $\lambda = 500$ nm; the shape of the meta-atom is given in the insets. The slope line labeled -2 in log-log representation shows the expected convergence law of the model.

Let us finally note that metasurfaces are usually described as surfaces made of an arrangement of resonant meta-atoms with subwavelength thickness and interatom distance; one of the advantages mentioned is that a large number of unit cells becomes possible even for a limited area [38]. For these metasurfaces, current or future, the numerical computation cost becomes more and more prohibitive when $d/\lambda \rightarrow 0$; interestingly, it is precisely in this limit that our model becomes increasingly predictive.

IV. TOWARD CURVED INTERFACES

In practice, metasurfaces are not infinite; in addition, they may be flexible [39]. The adaptation to homogenized models for flexible, curved metasurfaces was envisioned in [40,41] for arrays of particles that are the acoustic analog of perfect conductors and in [24] for light-penetrable particles (dielectric or metallic). It follows the intuitive idea that it is sufficient to replace the x and y derivatives in (2) by the normal and tangential derivatives, and this is expected to hold as long as the local radius of curvature R along the metasurface remains bigger than the array spacing d . In [24,40,41] the particles were nonresonant; here, we illustrate the validity of this extended model for resonant plasmonic metasurfaces.

We choose a metasurface with a fox-head-shaped contour containing 89 circular gold particles (radius = 10 nm, and spacing = 50 nm). The source is located within the fox's head of the form $S(\mathbf{x}, t) = s(\mathbf{x})e^{-i\omega t}$ (resulting in $\lambda = 400$ nm) with $s(\mathbf{x}) = 1$ within a disk centered at $\mathbf{x} = (0, -0.75)$ μm with a radius of 50 μm and $s(\mathbf{x}) = 0$ elsewhere; it is accounted for by solving $\Delta H + k^2 H = S$ in the harmonic regime. The solutions to the actual and effective problems are shown in Fig. 11. Note that, for curved meta-

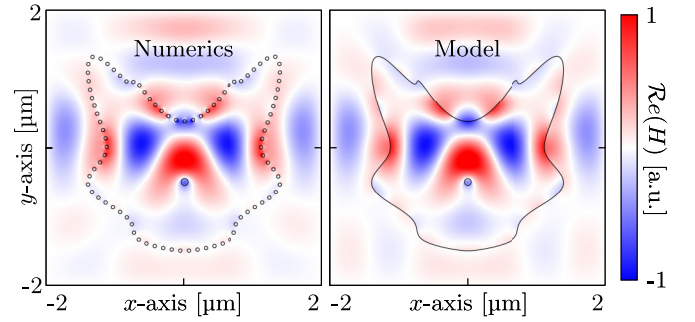


FIG. 11. Scattering by a closed, curved metasurface with circular gold particles along a fox-head-shaped curve (radius = 10 nm, $d = 50$ nm). Solutions are to the actual problem (left) and to the effective extended problem (right). At the boundaries of the square calculation domains, $H = 0$ is imposed.

surfaces, the solution to the effective problem has to be solved numerically as the translational invariance along the equivalent interface has been lost; to do this, the GSTCs were implemented in COMSOL MULTIPHYSICS following [24,42]. The agreement is good, which confirms that the extension of the model for a curved interface holds for resonant metasurfaces (in the reported case, we have $d/|R| < 0.7$).

We end this section by exemplifying the flexibility of the GSTCs when used in practical problems which may involve many scatterers, among which only some can be replaced by effective conditions (2). To do this, we symmetrically inserted in the fox's head two additional particles at $x = \pm 400$ nm and $y = -250$ nm. These particles are additional scattering elements that have to be accounted for explicitly in the effective problem (like in the actual one). The agreement between the two solutions remains very good, and the gain in the numerical cost is the same as in the previous case, as noted below.

The meshes used to solve the actual and effective problems in the cases reported in Figs. 11 and 12 are shown in Fig. 13. Each panel shows the mesh in the actual configuration for $x < 0$ and that in its effective counterpart for $x > 0$. In the actual problem, each individual particle along the array has to be resolved, and 600 000 degrees of freedom (DOFs) are

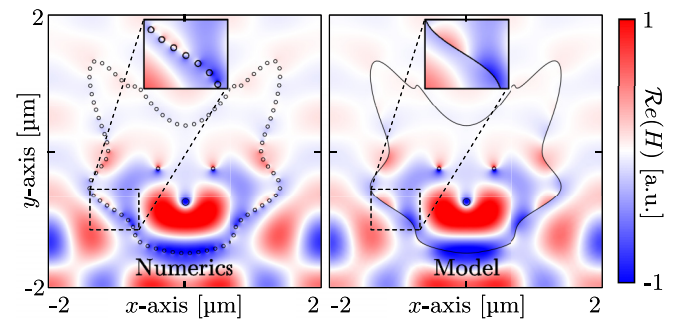


FIG. 12. Scattering by the same closed metasurface as in Fig. 11 with two additional isolated gold particles. The effective problem (right) combines GSTCs (2) instead of the array and the two isolated particles whose effect is accounted for explicitly (vanishing normal derivatives of H are imposed at the boundaries of the calculation domain). The insets illustrate the jump of H across the metasurface.

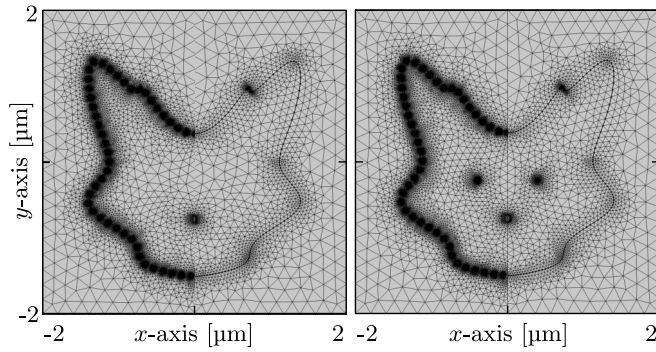


FIG. 13. Meshes used to solve the actual ($x < 0$) and effective ($x > 0$) problems whose results are shown in Fig. 11 (left) and Fig. 12 (right).

necessary to get a converged pattern. In contrast in the effective problem, only the variations of the underlying interface line have to be resolved, resulting in 10 000 DOFs. Next, the presence of the source and additional isolated particles produces the same local mesh refinements (resulting in the same ~ 4000 additional DOFs in the two cases).

V. CONCLUSION

We have obtained a homogenized model in which the effect of a plasmonic metasurface is encapsulated in GSTCs whose electrical susceptibilities are obtained from the solution of static elementary problems. The model was simplified by exploiting the decomposition of the elementary solutions into modes which are solutions of the plasmonic eigenvalue problem. Through numerical examples, the predictive strength of the model was discussed and illustrated by comparisons with direct FEM simulations. The extension of our study to two-dimensional plasmonic metasurfaces using the framework of [24] is straightforward and would lead to a significant reduction in the cost of the simulations, thus making the resolution of large plasmonic structures possible.

In its current form, our model considers a metasurface composed of a subwavelength unit cell, or pixels. Recent realizations built on this vision with the idea that if each pixel can be controlled independently, it becomes possible to realize programmable metasurfaces at the subwavelength pixel level [43–45] (not yet deeply subwavelength). By partially relaxing the periodicity assumption, such systems can be modeled with our approach [46]. Extensions of the model to other scenarios are also possible. If the thickness of the metasurface is no longer less than the wavelength as in [47], classical homogenization away from interfaces must be combined with interface homogenization, but this approach is limited to particles of invariant cross section along the interface [48,49]. Another extension that is more expensive and more difficult concerns metasurfaces formed by particles whose cross-sectional dimensions (and thus periodicity) are on the wavelength scale. It should be possible to perform a model reduction of the metasurface thickness and then to use multiscattering techniques to take into account propagation effects within and between particles. Finally, it is conceivable to incorporate quantum effects in systems with deeply nanoscale

characteristics, for which we should see the emergence of additional surface response functions, called Feibelman parameters [50,51].

ACKNOWLEDGMENTS

N.L. and A.M. acknowledge support from LABEX WIFI (Laboratory of Excellence within the French Program “Investments for the Future”) under References No. ANR-10-LABX-24 and No. ANR-10-IDEX-0001-02 PSL*. K.P. acknowledges support from the Agence de l’Innovation de Défense (AID) from the Direction Générale de l’Armement (DGA) under Grant No. 2019 65 0070 and the Agence Nationale de la Recherche under Grant No. ANR-19-CE08-0006. We warmly thank P. Lalanne, who, during a meeting of the GDR Ondes in Lille, attracted our attention to the interest in such homogenized models for application to plasmonic metasurfaces.

APPENDIX: ADDITIONAL RESULTS AND THE PEP DECOMPOSITION

The plasmonic eigenmode decomposition and the resulting expressions for the susceptibilities in (2) rely on the initial computation of the plasmonic eigenmodes and eigenvalues. The latter have to be determined primarily within a given range of permittivity, which is afterward associated with a given range of frequencies through Drude’s law (after the metal in the particle has been specified).

The accumulation of spurious eigenmodes near $\varepsilon = -1$ was shown and commented on in [25]; while accounting for these nonphysical modes does not affect the values of the scattering coefficients, a small region around $\varepsilon = -1$ has to be excluded because it artificially (and significantly) increases the computation time of the PEP calculation. For the eye-shaped particle (see Figs. 6 and 7), we computed the

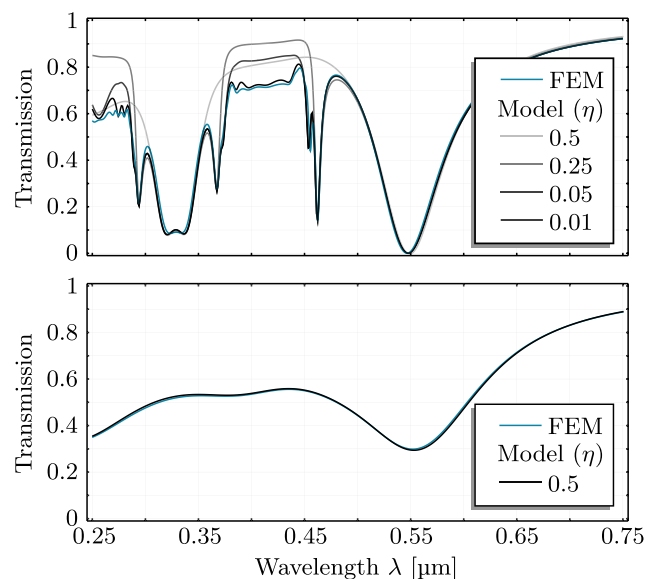


FIG. 14. Precision of the modal expansion based on the PEP when accounting for more modes around $\varepsilon = -1$ (see text) at $\theta = \pi/4$.

modes in the region $[\frac{1}{-10^{-2}}, \frac{1}{-1+\eta}[\cup]-1+\eta, -10^{-2}]$; with $\eta = 0.5, 10.25, 0.05$, and 0.01 , we found, respectively, 2, 4, 14, and 86 modes. In the last case, many modes are recognized as spurious modes (concentrated on a few nodes of the mesh) with negligible susceptibilities. In Fig. 14, we illustrate the increasing accuracy of the model when accounting for more (physical) modes. For artificially low losses, the sharp variations in the transmission are attributable to resonances with

high quality factors; hence, for modes close to $\varepsilon = -1$, it turns out that we must use small η values ($\eta = 0.01$) to see their effects. In contrast, when the actual losses are accounted for, resonances with a high quality factor are smoothed out; the remaining resonance with a low quality factor at $\lambda = 0.55 \mu\text{m}$ is associated with an eigenvalue far from $\varepsilon = -1$. As a result, with $\eta = 0.5$, the transmission curve is already faithfully reproduced.

-
- [1] S. A. Maier *et al.*, *Plasmonics: Fundamentals and Applications* (Springer, New York, 2007), Vol. 1.
 - [2] N. Meinzer, W. L. Barnes, and I. R. Hooper, Plasmonic meta-atoms and metasurfaces, *Nat. Photonics* **8**, 889 (2014).
 - [3] V. G. Kravets, A. V. Kabashin, W. L. Barnes, and A. N. Grigorenko, Plasmonic surface lattice resonances: A review of properties and applications, *Chem. Rev.* **118**, 5912 (2018).
 - [4] S. Zou, N. Janel, and G. C. Schatz, Silver nanoparticle array structures that produce remarkably narrow plasmon lineshapes, *J. Chem. Phys.* **120**, 10871 (2004).
 - [5] K. G. Cognée, H. M. Doleman, P. Lalanne, and A. Koenderink, Cooperative interactions between nano-antennas in a high-q cavity for unidirectional light sources, *Light: Sci. Appl.* **8**, 1 (2019).
 - [6] M. S. Bin-Alam, O. Reshef, Y. Mamchur, M. Z. Alam, G. Carlow, J. Upham, B. T. Sullivan, J.-M. Ménard, M. J. Huttunen, R. W. Boyd, and K. Dolgaleva, Ultra-high-q resonances in plasmonic metasurfaces, *Nat. Commun.* **12**, 974 (2021).
 - [7] J. Dai, F. Ye, Y. Chen, M. Muhammed, M. Qiu, and M. Yan, Light absorber based on nano-spheres on a substrate reflector, *Opt. Express* **21**, 6697 (2013).
 - [8] Y. Ra'di, C. R. Simovski, and S. A. Tretyakov, Thin Perfect Absorbers for Electromagnetic Waves: Theory, Design, and Realizations, *Phys. Rev. Appl.* **3**, 037001 (2015).
 - [9] K. M. Mayer and J. H. Hafner, Localized surface plasmon resonance sensors, *Chem. Rev.* **111**, 3828 (2011).
 - [10] J. Hu, D. Wang, D. Bhowmik, T. Liu, S. Deng, M. P. Knudson, X. Ao, and T. W. Odom, Lattice-resonance metalenses for fully reconfigurable imaging, *ACS Nano* **13**, 4613 (2019).
 - [11] X. Ni, A. V. Kildishev, and V. M. Shalae, Metasurface holograms for visible light, *Nat. Commun.* **4**, 2807 (2013).
 - [12] L. Huang, X. Chen, H. Mühlenbernd, H. Zhang, S. Chen, B. Bai, Q. Tan, G. Jin, K.-W. Cheah, C.-W. Qiu, J. Li, T. Zentgraf, and S. Zhang, Three-dimensional optical holography using a plasmonic metasurface, *Nat. Commun.* **4**, 2808 (2013).
 - [13] U. Laor and G. C. Schatz, The role of surface roughness in surface enhanced raman spectroscopy (SERS): The importance of multiple plasmon resonances, *Chem. Phys. Lett.* **82**, 566 (1981).
 - [14] B. Hopkins, D. S. Filonov, A. E. Miroshnichenko, F. Monticone, A. Alu, and Y. S. Kivshar, Interplay of magnetic responses in all-dielectric oligomers to realize magnetic Fano resonances, *ACS Photonics* **2**, 724 (2015).
 - [15] C. Sauvan, J.-P. Hugonin, I. S. Maksymov, and P. Lalanne, Theory of the Spontaneous Optical Emission of Nanosize Photonic and Plasmon Resonators, *Phys. Rev. Lett.* **110**, 237401 (2013).
 - [16] P. Lalanne, W. Yan, A. Gras, C. Sauvan, J.-P. Hugonin, M. Besbes, G. Demésy, M. D. Truong, B. Gralak, F. Zolla, A. Nicolet, F. Binkowski, L. Zschiedrich, S. Burger, J. Zimmerling, R. Remis, P. Urbach, H. T. Liu, and T. Weiss, Quasinormal mode solvers for resonators with dispersive materials, *J. Opt. Soc. Am. A* **36**, 686 (2019).
 - [17] P. Lalanne, W. Yan, K. Vynck, C. Sauvan, and J.-P. Hugonin, Light interaction with photonic and plasmonic resonances, *Laser Photonics Rev.* **12**, 1700113 (2018).
 - [18] M. Idemen, Universal boundary relations of the electromagnetic field, *J. Phys. Soc. Jpn.* **59**, 71 (1990).
 - [19] Y. Zhao, N. Engheta, and A. Alù, Homogenization of plasmonic metasurfaces modeled as transmission-line loads, *Metamaterials* **5**, 90 (2011).
 - [20] C. L. Holloway and E. F. Kuester, A homogenization technique for obtaining generalized sheet-transition conditions for a metafilm embedded in a magnetodielectric interface, *IEEE Trans. Antennas Propag.* **64**, 4671 (2016).
 - [21] B. Gallas, A. Maurel, J.-J. Marigo, and A. Ourir, Light scattering by periodic rough surfaces: Equivalent jump conditions, *J. Opt. Soc. Am. A* **34**, 2181 (2017).
 - [22] A. Pors, I. Tsukerman, and S. I. Bozhevolnyi, Effective constitutive parameters of plasmonic metamaterials: Homogenization by dual field interpolation, *Phys. Rev. E* **84**, 016609 (2011).
 - [23] H. Ammari, M. Ruiz, W. Wu, S. Yu, and H. Zhang, Mathematical and numerical framework for metasurfaces using thin layers of periodically distributed plasmonic nanoparticles, *Proc. R. Soc. A* **472**, 20160445 (2016).
 - [24] N. Lebbe, K. Pham, and A. Maurel, Stable GSTC formulation for Maxwell's equations, *IEEE Trans. Antennas Propag.* **70**, 6825 (2022).
 - [25] A.-S. B.-B. Dhia, C. Hazard, and F. Monteghetti, Complex-scaling method for the complex plasmonic resonances of planar subwavelength particles with corners, *J. Comput. Phys.* **440**, 110433 (2021).
 - [26] J.-J. Marigo, A. Maurel, K. Pham, and A. Sbiti, Effective dynamic properties of a row of elastic inclusions: The case of scalar shear waves, *J. Elasticity* **128**, 265 (2017).
 - [27] D. Grieser, The plasmonic eigenvalue problem, *Rev. Math. Phys.* **26**, 1450005 (2014).
 - [28] D. J. Bergman, Dielectric constant of a two-component granular composite: A practical scheme for calculating the pole spectrum, *Phys. Rev. B* **19**, 2359 (1979).
 - [29] D. J. Bergman, The dielectric constant of a simple cubic array of identical spheres, *J. Phys. C* **12**, 4947 (1979).
 - [30] P. Y. Chen, D. J. Bergman, and Y. Sivan, Generalizing Normal Mode Expansion of Electromagnetic Green's Tensor to Open Systems, *Phys. Rev. Appl.* **11**, 044018 (2019).

- [31] M. S. Agranovich, B. Z. Katsenelenbaum, A. N. Sivov, and N. N. Voitovich, *Generalized Method of Eigenoscillations in Diffraction theory* (Wiley-VCH, Verlag Berlin, 1999).
- [32] H. Van De Hulst, *Light Scattering by Small Particles* (Dover Publications, Inc. New York, 1981).
- [33] A. D. Rakić, A. B. Djurišić, J. M. Elazar, and M. L. Majewski, Optical properties of metallic films for vertical-cavity optoelectronic devices, *Appl. Opt.* **37**, 5271 (1998).
- [34] A. Akarid, A. Ourir, A. Maurel, S. Félix, and J.-F. Mercier, Extraordinary transmission through subwavelength dielectric gratings in the microwave range, *Opt. Lett.* **39**, 3752 (2014).
- [35] D. Doyle, N. Charipar, C. Argyropoulos, S. A. Trammell, R. Nita, J. Naciri, A. Pique, J. B. Herzog, and J. Fontana, Tunable subnanometer gap plasmonic metasurfaces, *ACS Photonics* **5**, 1012 (2018).
- [36] D. J. Bergman, P. Y. Chen, and A. Farhi, Scattering electromagnetic eigenstates of a two-constituent composite and their exploitation for calculating a physical field, *Phys. Rev. A* **102**, 063508 (2020).
- [37] P. Y. Chen, Y. Sivan, and E. A. Muljarov, An efficient solver for the generalized normal modes of non-uniform open optical resonators, *J. Comput. Phys.* **422**, 109754 (2020).
- [38] S. B. Glybovski, S. A. Tretyakov, P. A. Belov, Y. S. Kivshar, and C. R. Simovski, Metasurfaces: From microwaves to visible, *Phys. Rep.* **634**, 1 (2016).
- [39] J. Zhu, Z. Wang, S. Lin, S. Jiang, X. Liu, and S. Guo, Low-cost flexible plasmonic nanobump metasurfaces for label-free sensing of serum tumor marker, *Biosens. Bioelectron.* **150**, 111905 (2020).
- [40] B. Lombard, A. Maurel, and J.-J. Marigo, Numerical modeling of the acoustic wave propagation across a homogenized rigid microstructure in the time domain, *J. Comput. Phys.* **335**, 558 (2017).
- [41] B. Delourme, E. Lunéville, J.-J. Marigo, A. Maurel, J.-F. Mercier, and K. Pham, A stable, unified model for resonant Faraday cages, *Proc. R. Soc. A* **477**, 20200668 (2021).
- [42] N. Lebbe, S. Lanteri, S. Y. Golla, and P. Genevet, Susceptibility synthesis of arbitrary shaped metasurfaces, *Phys. Rev. B* **106**, 035110 (2022).
- [43] C.-W. Qiu, T. Zhang, G. Hu, and Y. Kivshar, Quo vadis, metasurfaces?, *Nano Lett.* **21**, 5461 (2021).
- [44] C. Meng, P. C. Thrane, F. Ding, J. Gjessing, M. Thomaschewski, C. Wu, C. Dirdal, and S. I. Bozhevolnyi, Dynamic piezoelectric MEMS-based optical metasurfaces, *Sci. Adv.* **7**, eabg5639 (2021).
- [45] C. Meng, P. C. Thrane, F. Ding, and S. I. Bozhevolnyi, Full-range birefringence control with piezoelectric MEMS-based metasurfaces, *Nat. Commun.* **13**, 2071 (2022).
- [46] K. Pham, N. Lebbe, and A. Maurel, Diffraction grating with varying slit width: Quasi-periodic homogenization and its numerical implementation, *J. Comput. Phys.* **473**, 111727 (2023).
- [47] A. V. Kabashin, P. Evans, S. Pastkovsky, W. Hendren, G. A. Wurtz, R. Atkinson, R. Pollard, V. A. Podolskiy, and A. V. Zayats, Plasmonic nanorod metamaterials for biosensing, *Nat. Mater.* **8**, 867 (2009).
- [48] J.-J. Marigo and A. Maurel, Second order homogenization of subwavelength stratified media including finite size effect, *SIAM J. Appl. Math.* **77**, 721 (2017).
- [49] F. Zhou Hagström, A. Maurel, and K. Pham, The interplay between Fano and Fabry–Pérot resonances in dual-period meta-gratings, *Proc. R. Soc. A* **477**, 20210632 (2021).
- [50] Y. Yang, D. Zhu, W. Yan, A. Agarwal, M. Zheng, J. D. Joannopoulos, P. Lalanne, T. Christensen, K. K. Berggren, and M. Soljačić, A general theoretical and experimental framework for nanoscale electromagnetism, *Nature (London)* **576**, 248 (2019).
- [51] Y. Liu, G. P. Wang, and S. Zhang, A nonlocal effective medium description of topological Weyl metamaterials, *Laser Photonics Rev.* **15**, 2100129 (2021).